The Electrochemical Society
Advancing solid state & electrochemical science & technology

OPEN ACCESS

Alkaline Electrochemical Reduction of a Magnesium Ferrospinel into Metallic Iron for the Valorisation of Magnetite-Based Metallurgical Waste

To cite this article: Daniela V. Lopes *et al* 2021 *J. Electrochem. Soc.* **168** 073504

View the article online for updates and enhancements.

244th **Electrochemical Society Meeting**

October 8 – 12, 2023 • Gothenburg, Sweden

50 symposia in electrochemistry & solid state science

Abstract submission deadline:
April 7, 2023

Read the call for papers & **submit your abstract!**

Alkaline Electrochemical Reduction of a Magnesium Ferrospinel into Metallic Iron for the Valorisation of Magnetite-Based Metallurgical Waste

Daniela V. Lopes,[1,2,z] Aleksey D. Lisenkov,[1] Sergii A. Sergiienko,[1] Gabriel Constantinescu,[1] Artur Sarabando,[1] Margarida J. Quina,[2] Jorge R. Frade,[1] and Andrei V. Kovalevsky[1]

[1]CICECO-Aveiro Institute of Materials, Department of Materials and Ceramic Engineering, University of Aveiro, 3810-193 Aveiro, Portugal
[2]University of Coimbra, CIEPQPF, Department of Chemical Engineering, Pólo II-Pinhal de Marrocos, 3030-790 Coimbra, Portugal

The electrochemical reduction of iron oxides in alkaline media arises as a novel approach for ironmaking and iron-rich waste valorisation. Strong advantages and attractive aspects of alkaline electroreduction include lower electric energy consumption, absence of CO_2 emissions, and non-polluting valuable by-products such as H_2 and O_2. Another potential advantage originates from the compatibility of this concept with intermittent renewable energies. However, to bring this technology to a competitive level, especially compared to the traditional steelmaking, innovative approaches and developments in materials processing and their appropriate integration into the electrolysis process are required. This research work explores the prospects for electrochemical reduction of a magnesium-containing ferrospinel, as a potential component in iron-containing wastes. The experimental approach considers bulk cathode- and suspension-based electrolysis concepts, which allow reaching 55% and 20% Faradaic efficiencies of the reduction to metallic iron, respectively. The effects imposed by the magnesium presence on the electroreduction kinetics, phase composition and morphology of the electroreduction products are evaluated and discussed. The obtained results open new perspectives for the recovery of metallurgical residues with low magnesium impurities content.

Electrolysis of iron oxides has been gaining interest as a greener alternative for the production of iron alloys and steel, without CO_2 emissions.[1,2] Metallurgical industries use iron oxides ores, such as the abundant magnetite, as raw materials for steel production. The electrochemical reduction of Fe(III) to metallic iron or zero-valent iron (ZVI, Fe^0) has been demonstrated from hematite suspensions[3–6] and hematite bulk samples as ceramic cathodes,[7–10] both in strong alkaline media. Magnetite (Fe_3O_4) is also an important intermediate phase for the bulk electrochemical reduction of hematite to ZVI/Fe^0,[7,9,10] allowing an increase of the cathodic current densities due to its relatively high electrical conductivity (10^{-14} S cm^{-1} for hematite and 10^2 S cm^{-1} for magnetite, respectively, at room temperature[11]). Despite little studied, the electroreduction of Fe_3O_4 to Fe^0 also represents an interesting approach towards the restoration of corroded iron and steel surfaces, magnetite ores and magnetite-based waste recycling, e.g. metal scraps and metallurgical slags. Moreover, iron oxide ores and rocks may also be considered as raw material for the electroreduction to Fe^0 when considering, for example, chromite ores[12] or saprolite rocks.[13] Acidic conditions were tested at room temperature for the electroreduction of Fe_3O_4 bulk samples with carbon,[14–16] revealing Fe(II) ions dissolution in sodium perchlorate electrolyte (1 M) as an intermediate step. Deposited magnetite films on a silver substrate were electroreduced to epitaxial Fe^0 films under alkaline conditions (2 M of NaOH), from 25 to 80 °C.[17] However, the solid-state transformation of Fe_3O_4 to Fe^0 has not been proved so far. Instead, when stronger alkaline conditions were tested with bulk porous magnetite pellets (10 M of NaOH, 22 to 90 °C[18]) and in suspension (18 M of NaOH, 110 °C[19]), both studies considered the dissolution of Fe_3O_4 into Fe(II) species as $Fe(OH)_3^-$ in the electrolyte. Faradaic efficiencies of the electrochemical process were up to 85% for bulk porous samples[18] and ≈5% in suspension.[19] However, more studies are

required to ascertain the electrochemical reduction pathway of Fe_3O_4 in both systems.

Besides iron oxides, metallurgical slags usually contain considerable amounts of MgO, Al_2O_3, SiO_2 and CaO, where MgO can represent around 6.3 to 12.6 wt%, depending on the industry.[20,21] When pursuing electrochemical reduction studies, the order of complexity of the metallurgical waste can be decreased by mimicking the main components of the waste, as a first approach. Thus, one can consider the incorporation of some potential contaminants, which can be introduced in the magnetite/hematite structure. In fact, several cations such as Mg, Al, Ti, Ni and Cr, have been investigated in this respect, when seeking improved redox stability and high-temperature refractoriness in spinels.[22–26] Despite the lower electrical conductivity when compared to pure Fe_3O_4, one can improve the electrical conductivity in $MgFe_2O_4$ ceramics (10^{-3} S cm^{-1} at 600 °C[27]) by partially substituting the Fe(II) ions from the octahedral lattice with Mg(II), such as for $Fe_{2.3}Mg_{0.7}O_4$ (15 S cm^{-1} at room temperature[24]). The transport properties and redox behaviour of $Fe_{3-x}Mg_xO_4$ spinels are also relevant for prospective applications such as gas sensors,[28] catalysis,[29] electrodes for the electrochemical reduction of NO_x,[27] solar thermochemical fuel production[30] and as anodes for pyroelectrolysis of molten salts.[31] However, complete electrochemical reduction of $Fe_{3-x}Mg_xO_4$ spinels to metallic Fe^0 in strongly alkaline conditions has not been attempted.

The present work is devoted to the electrochemical reduction of a porous $Fe_{2.3}Mg_{0.7}O_4$ spinel, processed following the guidelines obtained in Ref. 32. A particular attention is given to the comparison between the cathodic electroreduction processes in bulk and suspension approaches. The relevant effects of the magnesium presence in the samples subjected to electroreduction were investigated for the first time, aiming at the valorisation and recycling of magnetite-based metallurgical wastes.

Experimental

Hematite (Gute Chemie, abcr GmbH, 99.8%) and magnesium oxide (Sigma-Aldrich, −325 mesh, 99+%) were used as the precursors to

produce porous $Fe_{2.3}Mg_{0.7}O_4$ ceramics. The ceramic samples were processed by the route described in Ref. 32 including preliminary thermal pre-treatment and milling of the precursors to improve the homogeneity, followed by the emulsification with liquid paraffin and final firing at 1400 °C in argon atmosphere (2 h dwell and 5 °C min^{-1} heating/cooling rates). Open porosity of ceramic pieces was assessed by Archimedes methodology as performed in Refs. 10, 32, 33.

The electrochemical reduction testings of the $Fe_{2.3}Mg_{0.7}O_4$ samples was performed considering both bulk and in suspension forms. The electrochemical tests were performed at 90 °C in a 10 M NaOH solution, used as electrolyte (PTFE reactor, 100 ml of electrolyte). A Hg|HgO|NaOH (1 M) (+0.098 V vs saturated hydrogen electrode) was used as a reference electrode (RE). The RE and electrolyte were connected using a Luggin capillary. Spiral-wound platinum wire (7.40 cm^2) was used as a counter electrode (CE). For the bulk reduction, porous $Fe_{2.3}Mg_{0.7}O_4$ ceramic cathodes were polished up to a 2 mm thickness and glued with silver paste (Agar Scientific) to a Nickel-grid (30 mm height × 10 mm width × 0.45 mm thickness, with a 0.90 mm aperture and and a Ni wire diameter of 0.22 mm). The configuration of the bulk working electrode (WE) was similar to the one described elsewhere,[34] in an NMAg-R configuration. The outer area of the Ni grid in contact with the electrolyte solution was painted with lacquer (Lacomit Varnish, Agar Scientific) to prevent any unwanted electrochemical contributions. A similar but bare Ni grid (4 cm^2) was used as WE for the electrochemical reduction in suspension. In this case, the same processed ceramics were crushed into powder (<90 μm). The ceramic suspension with a concentration of 110 g l^{-1} in 10 M NaOH was used as an electrolyte in this case. During the electrochemical tests, the electrolyte was mechanically stirred (100 rpm) by a Heidolph RZR 2020 apparatus with a PTFE rod and blades. Particle size distribution analysis of the $Fe_{2.3}Mg_{0.7}O_4$ spinel powder, after crushing, was performed with a Coulter LS 230 (0.040–2000 μm) equipment.

A VersaSTAT 4 (AMETEK) potentiostat was used for the electrochemical studies, which included a cyclic-voltammetry analysis between -1.3 V to 0 V, with a scanning rate of 10 mV s^{-1}. The electrochemical reduction was performed for 6 h in potentiostatic mode (-1.14 V). Electrochemical impedance spectra (EIS) were registered only in the case of the bulk reduction, in a frequency range of 1 Hz to 1 MHz, 50 mV of amplitude and 50 points per decade. All samples were washed with distilled water and ethanol after the electrochemical tests, and posteriorly dried in a vacuum desiccator. Faradaic efficiencies were calculated considering the mass differences of the WEs before and after the electrochemical processes, as well as the total electric charge passed in the electrochemical cell and the iron content (Fe^0) obtained by the X-ray diffraction (XRD) technique.

The microstructural studies of as-prepared samples and corresponding post-mortem analysis after the electrochemical reduction were performed by scanning electron microscope (SEM, Hitachi SU-70), combined with energy disperse spectroscopy analysis (EDS, Bruker Quantax 400). The phase composition was identified by XRD, using a PANalytical XPert PRO diffractometer (CuKα radiation, $2\theta = 10°$–$80°$) equipped with a graphite monochromator, along with the Panalytical HighScore Plus 4.7 (PDF-4) software.

Results and Discussion

General characterisation of the bulk and powdered $Fe_{2.3}Mg_{0.7}O_4$ ceramics.—Microstructural features of the $Fe_{2.3}Mg_{0.7}O_4$ spinel are represented in Fig. 1. The emulsification process resulted in the formation of well-defined cellular structures (Fig. 1A), with an open porosity of 44 ± 1%. The open porous structure with suitable interconnection channels between the cells (Fig. 1B) is proved to play an important role in the electrochemical reduction, facilitating the electrolyte access inside the bulk ceramic cathode. For the electrochemical tests performed in suspension, the cellular ceramics were

crushed into powder, as shown in Fig. 1C; in this last micrograph, smaller fragments can be observed together with larger particles. The size distribution analysis results suggest an average particle size of around 36 μm. The D_{10}, D_{50} and D_{90} values were, respectively, 5.7 μm, 22.7 μm and 86.4 μm. A single-phase composition of the prepared magnetite-based spinel can be clearly seen in the XRD pattern from Fig. 1D. This result is in agreement with the phase diagram of Fe_2O_3–MgO.[35]

Bulk electrochemical reduction.—Figure 2 shows the cyclic-voltammograms (CV) curves obtained before (t = 0 h) and after (t = 6 h) the electrochemical tests performed on the bulk spinel ceramic cathode. Higher current densities can be observed for t = 0 h, when compared to other studies performed on porous hematite-based materials,[10,34] due to the superior electrical conductivity of our $Fe_{2.3}Mg_{0.7}O_4$ samples. The reduction of Fe_3O_4 to aqueous Fe(II) species is usually considered before the reduction to Fe^0.[10,18,34,36,37] Monteiro et al.[18] observed a single and sharp cathodic peak at -1.16 V, ascribed only to the Fe^0 nucleation due to the reduction of a dense Fe_3O_4 pellet at 90 °C (10 M of NaOH). In the present work, a single and broad cathodic peak (C) is observed due to the reduction to Fe^0 at ≈ -1.11 V. However, the relatively low cathodic potential of the C onset (-0.56 V) is associated with the combined reduction of Fe(III) to Fe(II) and, later on, to Fe^0. The simultaneous presence of redox-stable Mg^{2+} ions that may form as a compensation to the reduction of the spinel phase, may result in a partial blocking of the active electrochemical sites and delayed electrochemical response. One should also note that the $Fe_{2.3}Mg_{0.7}O_4$ structure is characterised by a different Fe(II):Fe(III) ratio as compared to Fe_3O_4 (0.3:2 against 1:2), implying an excess of Fe (III). Two clear anodic peaks, A_1 (-0.84 V) and A_2 (-0.40 V), can be observed in Fig. 2. While the first one can be ascribed to the oxidation of Fe^0 to Fe(II) species, such as $Fe(OH)_3^-$ and mostly $HFeO_2^-$, in agreement with Ref. 18 a shift of ≈ 0.2 V is clearly visible for the $Fe_{2.3}Mg_{0.7}O_4$ spinel in the case of A_2, as compared to a similar peak observed also in Ref. 18. For instance, the oxidation potential to Fe(III) species was around -0.6 V in Ref. 18 while another anodic peak at -0.4 V was found only in the case of lower electroreduction temperatures (22 °C and 50 °C). Although the unambiguous assignment of this peak was impossible, it was assumed that it might be related to the formation of Fe (III) oxides and hydroxides, passivating the electrode surface. The corresponding delay in the electrochemical response observed in the present work can be related to the formation of magnesium-containing low-soluble species, providing a similar passivating effect. Higher current densities were observed after 6 h of reduction, indicating the presence of more conductive phases, such as Fe^0, after the reduction. The broad anodic peaks, similar to those mentioned above, were observed at -0.64 V (A'_1), -0.28 V (A'_2), together with a shoulder at -0.97 V (C').

The chronoamperometry curve showing the evolution of the $Fe_{2.3}Mg_{0.7}O_4$ spinel cathode reduction during 6 h is shown in Fig. 3. Each period corresponds to a continuous electroreduction process, with intervals for electrochemical impedance spectroscopy (EIS) measurements (Fig. 4). The applied potential corresponded to slightly more cathodic conditions, as compared to the peak C (Fig. 2). The chronoamperometry curve shown in Fig. 3 is in fair agreement with the three-phase interlines (3PIs) model, suggested for the electrochemical reduction of both dense and porous bulk hematite electrodes, in similar systems.[9,34] The formation of an interface between the current collector|pellet|electrolyte is enabled by the entrance of the electrolyte inside the porous cavities, leading to the initial decrease of the cathodic current density. Further electroreduction is accompanied by the formation of metallic Fe^0, and results in a gradual increase of the current density. The current density increases until the end of 6 h reaching a maximum of around 51.3 mA cm^{-2}. Kinetics limitations do not allow the complete electroreduction of the spinel cathode. Therefore, a further decrease of the current after attaining its maximum was not observed. Despite the 3PIs model has
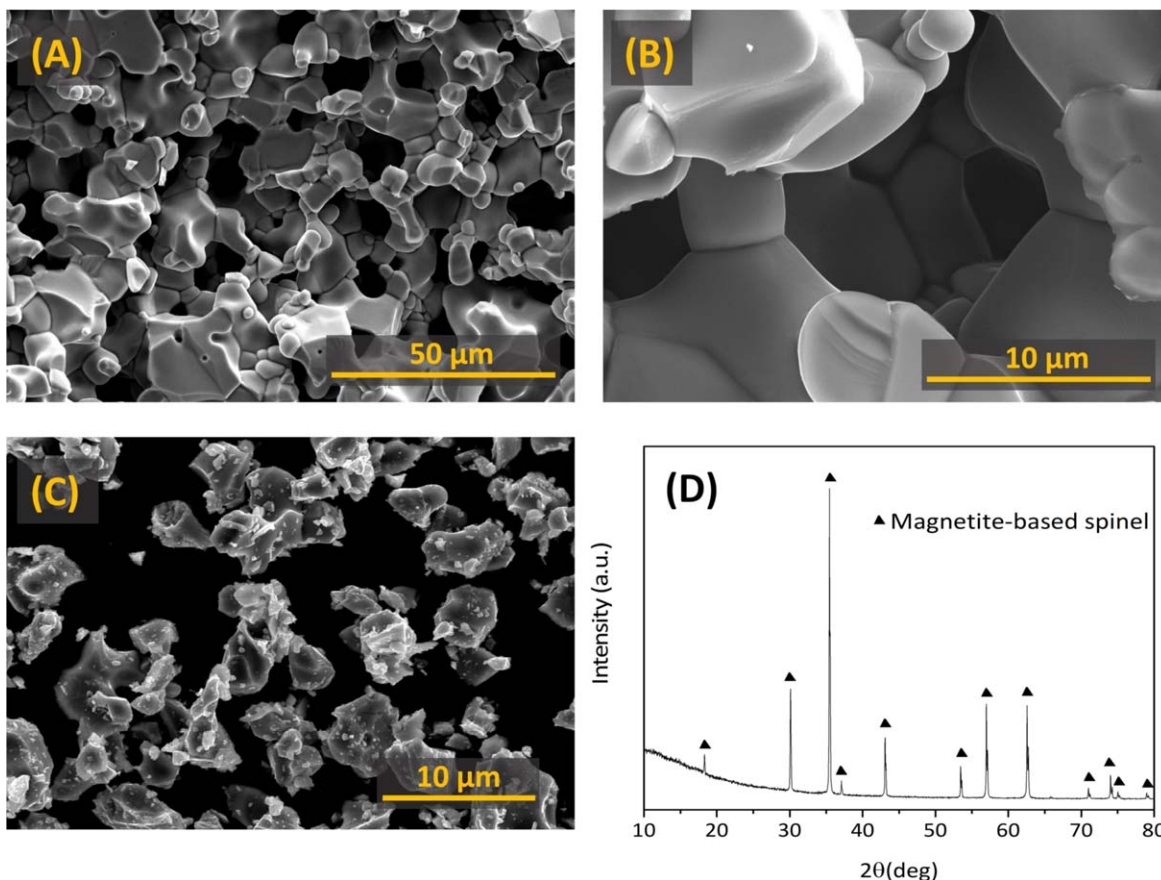
Figure 1. SEM micrographs of the $Fe_{2.3}Mg_{0.7}O_4$ spinel (1400 °C, argon atmosphere): (A) porous ceramic, (B) percolation channel inside of a pore, (C) fractured ceramic piece; (D) powder XRD pattern.
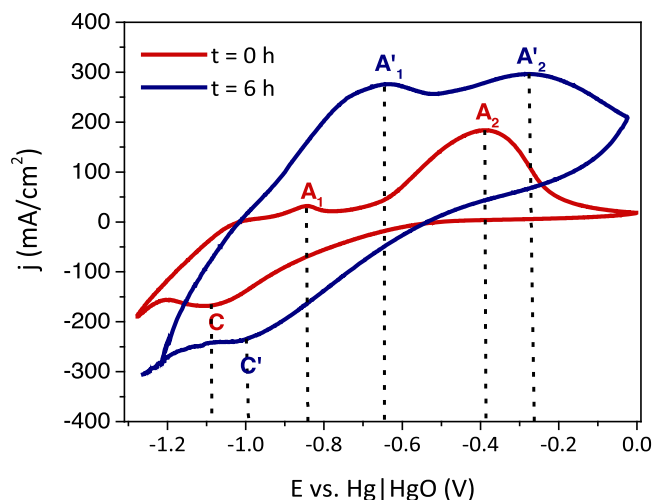

Figure 2. CV curves recorded at 10 mV s^{-1} before (red line) and after 6 h (blue line) of the electroreduction (90 °C, 10 M).
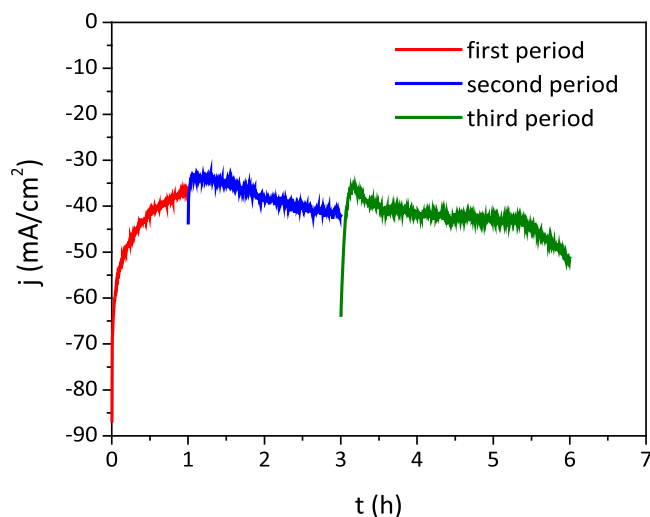

Figure 3. Chronoamperometry curves of the $Fe_{2.3}Mg_{0.7}O_4$ electrochemical reduction in bulk during 6 h (90 °C, 10 M). The reduction was performed at 1.14 V.

been applied mainly for insulating materials (e.g. Fe_2O_3), the tendency of the curve from Fig. 3 clearly indicates a similar behaviour, but for more conductive materials, such as $Fe_{2.3}Mg_{0.7}O_4$.

The EIS studies are illustrated by the Nyquist plots from Fig. 4, revealing strongly depressed and poorly-resolved semi-circles in the high-frequency range, followed by other depressed semi-circles at lower frequencies. Beyond the limitation of the frequency range of the equipment, the first depressed arc can also be associated with the behaviour of porous materials, specially at high frequencies[38] The

second depressed semi-circle might correspond to a mixture of diffusion mechanisms combined with the charge transport from the electrolyte to the WE. Several overlapped processes with distinct relaxation times can contribute to the observed depressed shape.[39] Due to the high complexity of extracting the relevant information related to the several electrode diffusion mechanisms, the WE contribution was not analysed. However, one can opt to use a typical $R_s(R_{dl}Q_{dl})(R_{WE}Q_{WE})$ equivalent circuit between the RE and WE for the de-convolution of the main
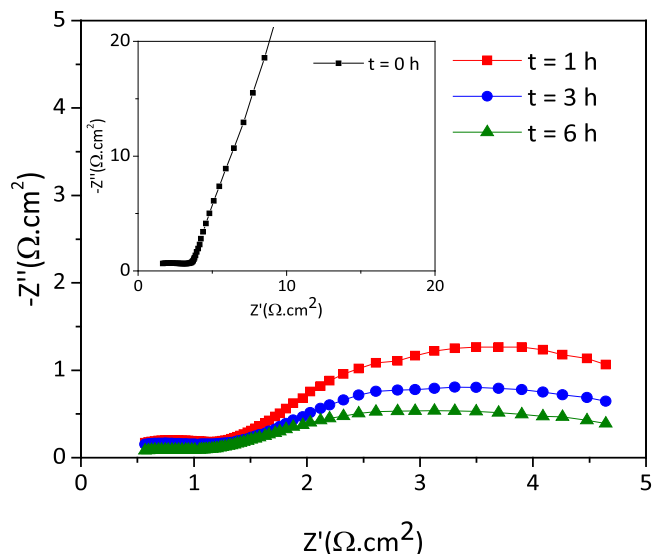
Figure 4. EIS spectra (Nyquist plots) for non-reduced samples (t = 0 h) and samples after 1, 3 and 6 h of electroreduction.

contributions related to the double layer mechanism to ensure a suitable fitting of the first semi-circle. The components of the mentioned equivalent circuit include the resistance of the electrolyte (R_s), the charge transfer resistance of the double-layer (R_{dl}), the double-layer capacitance (Q_{dl}), and the resistive and capacitive contributions of the working electrode (R_{WE}, Q_{WE}).

Table I shows the main EIS spectra parameters extracted during fitting. The typical R_s values obtained for the non-reduced sample and 1 h reduced ceramic cathode are similar to those obtained for Fe_3O_4 from Ref. 18 and indicate a low ohmic resistance between the RE and WE. The R_s values obtained from the EIS spectra after 3 and 6 h electroreduction are vanishing, suggesting other possible contributions at higher frequencies. In particular, the reduction process is accompanied by shrinkage due to the higher density of the Fe^0 as compared to the initial spinel. This promotes the formation of additional porosity, which in turn may provide an additional contribution at higher frequencies.[38]

A decline of the depression factor "n" is also observed during electroreduction, as evidence of the overlapping processes. The general tendency of R_{dl} and Q_{dl} is to decrease and increase with time, respectively, indicating the conversion of the spinel material to a more conductive phase, most likely Fe^0, as in Refs. 18, 34. The true capacitance (C_{dl}, Eq. 1) values, calculated as in Refs. 40, 41 are typical for the double layer interface between the electrolyte and WE. After 1 h of electroreduction, the large C_{dl} increase is also related to the growth and nucleation of new Fe^0 crystals at the surface of the WE, as in Ref. 18

$$C_{dl} = \frac{(R \times Q_{dl})^{1/n}}{R} \quad [1]$$

The presence of metallic iron (23 ± 4 wt%) was unambiguously confirmed by post-mortem XRD analysis of ceramic cathodes after

6 h of electroreduction (Fig. 5A). The initial composition (magnetite-based spinel) and traces of magnesium hydroxide phase (2 ± 1 wt%) can also be observed. Most likely, the magnesium hydroxide is predominantly amorphous, as suggested by the presence of a hump from the low angles region of the diffractogram. The existence of $Mg(OH)_2$ is also in agreement with the Pourbaix diagram of magnesium species in aqueous solutions.[42] The typical cellular morphology of the porous spinel can still be observed after the electrochemical reduction, as shown in Fig. 5B. In this case however, a $Mg(OH)_2$ layer (coloured as blue in the EDS mapping images) appears to cover its surface, in agreement with the previous discussion on the electrochemical data. On the other hand, Fe^0 crystals ($\approx \mu m$ of diameter and $\approx \mu m$ of length; coloured as red in EDS mapping images) seem to grow through the $Mg(OH)_2$ layer as a dendrite vertex-shape in the wide open pores regions. The Fe^0 crystals shown in the figure are likely formed by significantly smaller and aggregated particles ($\approx$10 nm).

The morphology of the reduced ceramic cathodes as a function of the distance from the current collector (CC) is shown in Fig. 6. Contrary to the previous study focused on bulk $Fe_{2-x}Al_xO_3$ composition,[34] Fe^0 crystals are observed not only near the CC (Fig. 6A), but are also clearly identified even relatively far from the CC (Fig. 6B) and even at the surface exposed to the electrolyte (Fig. 6C). This apparent easiness of the electroreduction is most likely promoted by the higher electrical conductivity of the $Fe_{2.3}Mg_{0.7}O_4$ spinel as compared to hematite-based WEs. Furthermore, crystal growth seems to be limited because of this particular morphology. Inside the bulk WE, the Fe^0 crystals are restrained to the dimensions of the porous cavities. Once the surface is directly exposed to the electrolyte, the Fe^0 crystals start to demonstrate a significant growth in elongated shapes (Fig. 6D) due to fewer spatial restrictions.

The electrochemical mechanism of the $Fe_{2.3}Mg_{0.7}O_4$ reduction is, in fact, a dissolution-redeposition process. Part of the Fe(III) is reduced and dissolved to aqueous Fe(II) species, mainly as $Fe(OH)_3^-$ and $HFeO_2^-$, to the electrolyte inside the porous cavities. At the same time, Mg^{2+} cations are dissolved in the NaOH electrolyte solution and precipitate as $Mg(OH)_2$, blocking the surface from further reduction. The dissolution of Mg^{2+}-containing species itself is promoted by electroreduction, which destroys the host spinel structure. When the aqueous Fe(II) species are reduced, the Fe^0 may be redeposited on top of the $Mg(OH)_2$ layer. This partial coverage has a direct impact on the Faradaic Efficiency of the electrochemical process, along with the hydrogen evolution reaction (HER). HER is a known side reaction due to the water splitting at sufficient cathodic polarizations, close to those required for the conversion of Fe(II) species to Fe^0.[3,10,18] While 85% of efficiency was obtained in Ref. 18 with porous Fe_3O_4 (45% open porosity) in similar conditions, 55 ± 10% was obtained in the present investigation, in the case of a magnesium-containing magnetite.

Electrochemical reduction in suspension.—The electrochemical deposition of Fe^0 was performed using a Ni grid (WE) in the same experimental conditions as for the bulk electroreduction. Figure 7 shows the chronoamperometry curve obtained during electroreduction, when applying the same cathodic potential as for the bulk (−1.14 V), for the sake of comparison. A gradual increase in current density up to 13.6 mA cm^{-2} is observed, mostly due to the

Table I. Fitting aspects of EIS data.

Time	R_s ($\Omega.cm^2$)	R_{dl} ($\Omega.cm^2$)	n	Q_{dl} ($\mu F \, cm^{-2}$)	C_{dl} ($\mu F \, cm^{-2}$)
t = 0 h	0.21	3.82	0.43	3.36×10^3	9.80
t = 1 h	0.16	1.30	0.36	2.50×10^4	58.02
t = 3 h	$\sim 10^{-6}$ a)	1.53	0.26	4.81×10^4	31.01
t = 6 h	$\sim 10^{-7}$ a)	1.28	0.23	$9.80 \times \times 10^4$	29.32

a) Values out of the expected range, indicating the inadequacy of the selected equivalent circuit for the fitting of high-frequency impedance data.
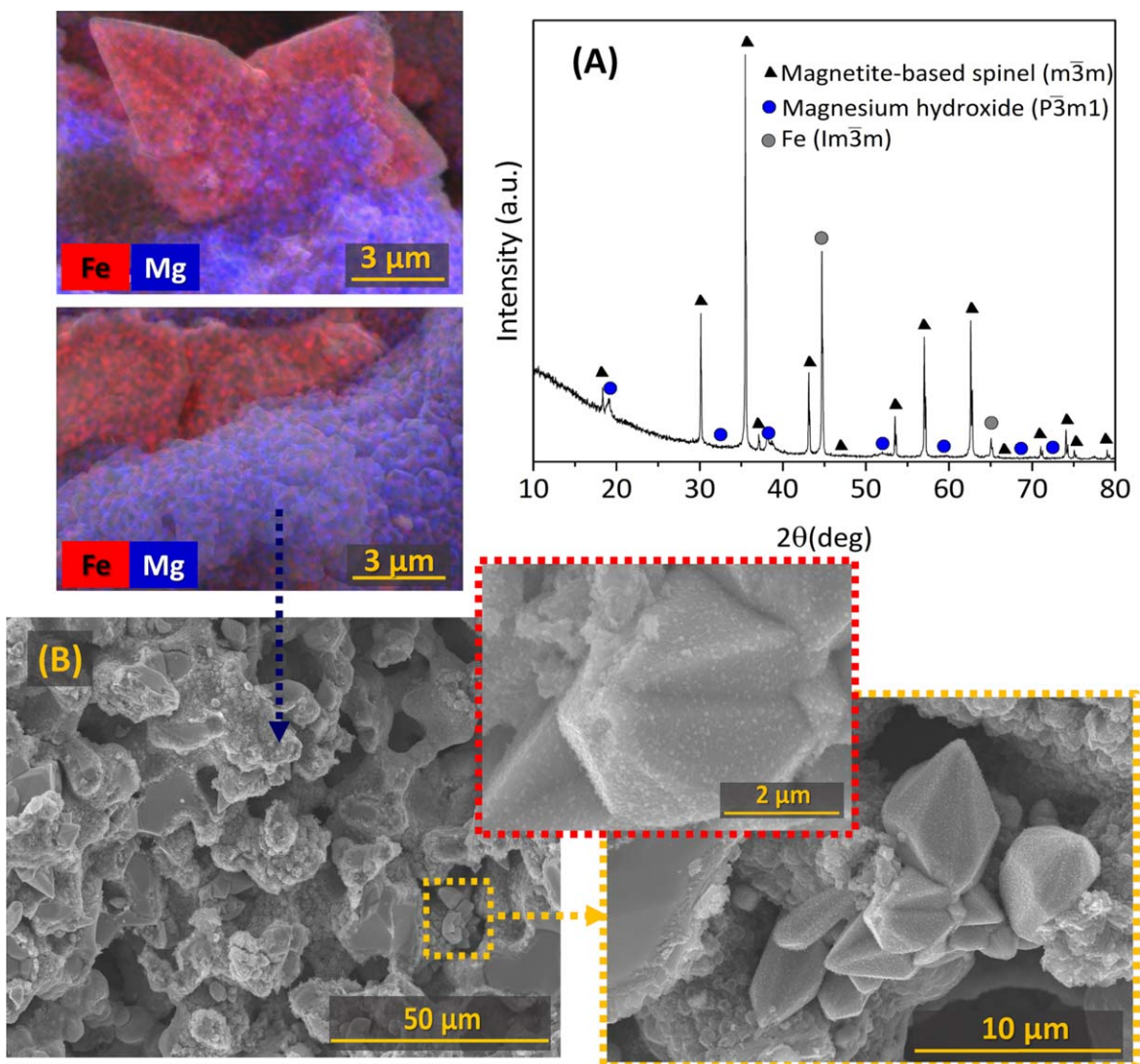
Figure 5. Results of the post-mortem analysis after 6 h of electroreduction: (A) XRD pattern; (B) SEM/EDS images.

increase of the electrode effective surface area, boosted by Fe^0 electrodeposition. Although this aspect is still under debate in literature, the electroreduction of iron oxides in alkaline suspensions is mostly contributed by an active interplay between the particles adsorption at the WE's surface[43,44] and the dissolution of iron species from the particles to the electrolyte.[4,19,45] The work conducted in alkaline suspensions has been mainly focused on hematite-based materials. When using a suspension of a spinel material, one still expects the dissolution of the Fe(III) and Fe(II) as its hydrated forms, $Fe(OH)_4^-$ and $Fe(OH)_3^-$, respectively. The aqueous $Fe(OH)_3^-$ is further reduced to Fe^0 and deposited at the surface of the WE. Magnetite solubility is about 5×10^{-3} M in alkaline aqueous solutions, while $Fe(OH)_4^-$ is expected to present a solubility of around the same order of magnitude ($\approx 10^{-3}$ M) for temperatures around 110 °C.[19] Due to the low solubility of the iron oxide materials, the contribution of the mentioned iron dissolution for electrodeposition is expected to be limited, justifying the relatively slow progress of the electroreduction current at a fixed cathodic potential (Fig. 7).

The CV curve obtained after 6 h of electroreduction is shown in Fig. 8. No contribution of the redox reactions involving nickel were observed before the deposition, since anodic potentials higher than 0.3 V are required for Ni oxidation.[46] After 6 h (Fig. 7), lower current densities were observed when comparing with the reduction in bulk (Fig. 2). The latter suggests that the adsorption of the spinel

particles at the WE surface for subsequent electrochemical reduction represents a limiting step. A sharp cathodic peak C_2 is visible at -1.08 V with an onset potential at -1.03 V, associated with the potential for the reduction to Fe^0. Similarly to the anodic peaks observed for the bulk system, A^* (-1.03 V) and A_3 (-0.89 V) are in the expected range for the oxidation of Fe^0 to Fe(II) species (FeO, $Fe(OH)_3^-$ and $HFeO_2^-$), while shoulder A_4 (-0.60 V) might be related to the oxidation to Fe_3O_4 and/or FeOOH. The position of the A_4 peak also agrees very well with the results on bulk electrochemical reduction of Fe_3O_4[18]. The similarities in CV response observed for the $Fe_{2.3}Mg_{0.7}O_4$ reduction in suspension and bulk electroreduction of Fe_3O_4[18] may indicate that the presence of magnesium-containing species and corresponding effects are less critical in the suspension. More guidelines can be obtained from the microstructural data and phase composition of the deposits obtained by the electroreduction in suspension.

The microstructural features of the iron-based species deposited on the Ni grid are shown in Fig. 9. The grid is covered with needles ($\approx 3 \ \mu m$ of diameter) and other smaller particles showing a preferential orientation; significant porosity is also visible (Fig. 9A and B). The Fe^0 crystals resemble dendritic structures, as previously observed for the $Fe_{2-x}Al_xO_3$ alkaline suspensions.[47] However, the crystals appear to be thinner (≈ 13 to $18 \ \mu m$ in diameter[47]), fragile and with less developed dendrites in most cases. Their morphology is likely linked to the current densities during the electroreduction,
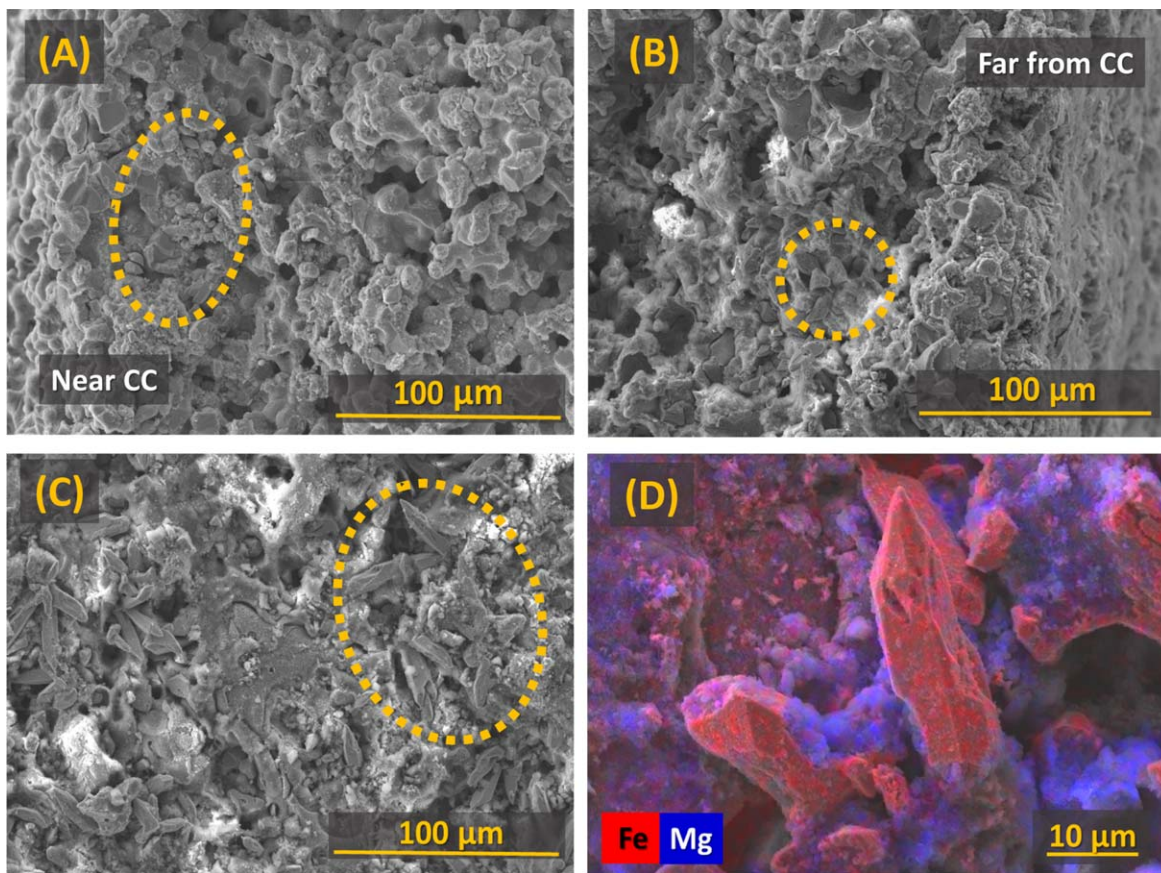
Figure 6. SEM micrographs of the spinel cathode after 6 h of electroreduction: (A) near the CC; (B) far from CC; (C) surface of the sample exposed to the electrolyte (opposite side of CC); (D) EDS map of Fe^0 crystals at the surface of the sample.
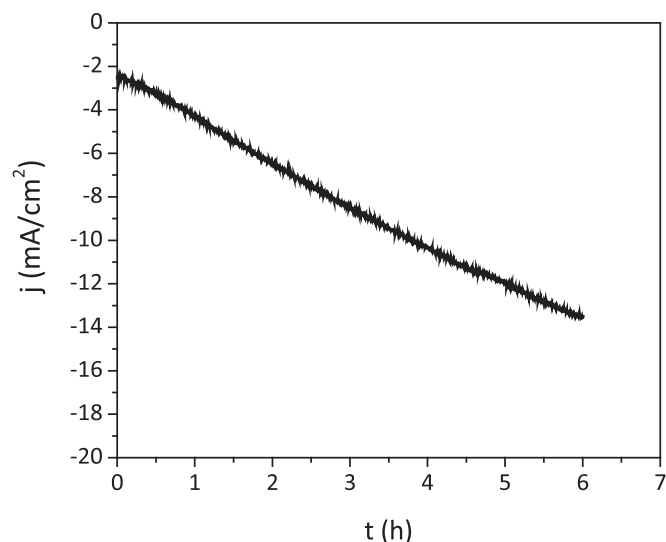

Figure 7. Chronoamperometry curve during the 6 h of the Fe$_{2.3}$Mg$_{0.7}$O$_4$ electroreduction in alkaline suspension (90 °C, 10 M).

Figure 8. CV curve recorded at 10 mV s^{-1} after the electrochemical deposition (90 °C, 10 M).

showing to be different from that in Ref. 47. Poorly-defined crystallites were also found for Fe$_3$O$_4$ suspension in Ref. 19 in different experimental conditions (18 M of NaOH, 110 °C, −1.66 V). Distinct and finer microstructures can also be seen in Fig. 9B. EDS mapping results (Fig. 9C) reveal the presence of Mg-containing species in the iron deposits, also confirmed by the XRD analysis (Fig. 9D). However, in this case, their amount appears to be lower than in the case of the bulk reduction (Fig. 5), where the
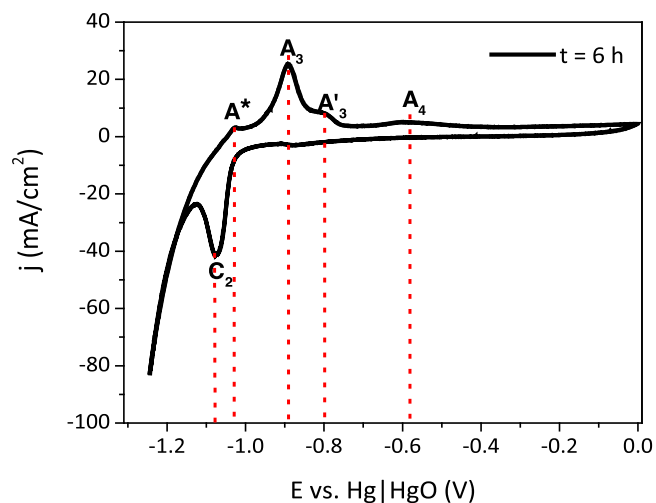
diffusion and dissolution of Mg^{2+} compounds inside the porous structure are limited. Secondly, the XRD results also show that the deposits contain initial Fe$_{2.3}$Mg$_{0.7}$O$_4$ spinel inclusions trapped from the suspension. These inclusions may contribute to the presence of several anodic peaks in the CV curves obtained in the case of the electroreduction in suspensions (Fig. 8).

It should be noted that, when comparing the electroreduction of Fe$_2$O$_3$ and Fe$_3$O$_4$, Feynerol et al. [19] obtained a lower Faradaic efficiency with Fe$_3$O$_4$ suspension (5% against 86%). This phenomenon
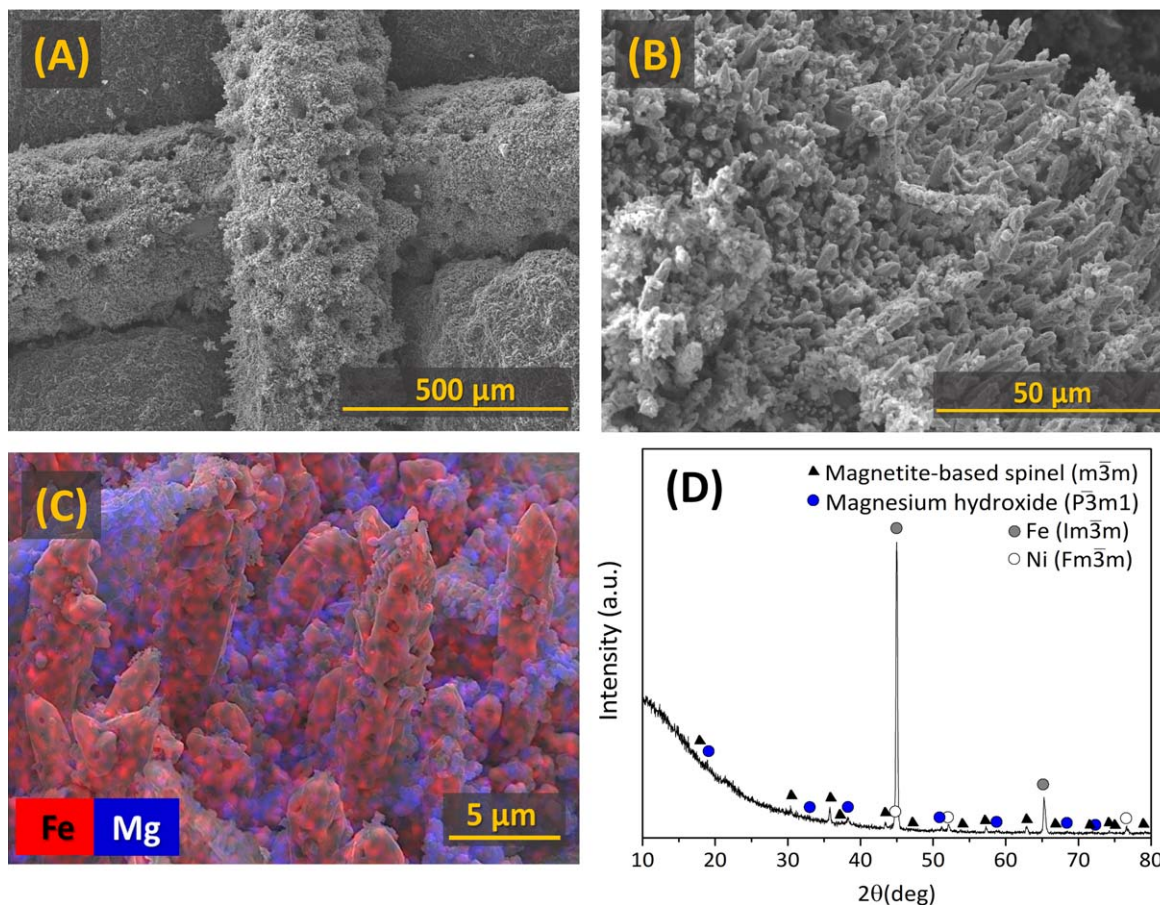
Figure 9. SEM/EDS images of the Fe^0 deposits on the Ni-grid WE from the spinel suspension after 6 h of electroreduction: (A), (B) and (C); (D) XRD pattern of the WE deposit after the electroreduction.

was attributed to two main reasons including the higher cathodic polarizations required for Fe_3O_4 suspensions, consequently leading to higher HER and to its magnetic behaviour on stirring, leading to concentration gradients in the suspension. The last effect was minimized in the current work by using mechanical stirring with PTFE blades. The latter probably also contributed to achieving the Faradaic efficiency of the reduction to metallic iron reaching 20 ± 2%, which is almost 4 times higher than the one obtained in Ref. 19.

Conclusions

The electrochemical reduction of the $Fe_{2.3}Mg_{0.7}O_4$ spinel to metallic iron was attempted for the first time in both bulk- and suspension- based cathode approaches, under strongly alkaline conditions (10 M NaOH). Bulk porous samples (44%) processed by ceramic suspension emulsification using liquid paraffin acted as ceramic working electrodes. The presence of Mg in the spinel composition was found to affect the electroreduction process in both bulk and suspension scenarios. Although the porous cathode structure was proved to facilitate the entrance and diffusion of the electrolyte, it was not sufficient to provide appropriate dissolution of the Mg^{2+}-containing species formed during electroreduction, resulting in a partial blocking of the electrochemically active surface and appearance of kinetic limitations. Nevertheless, quite promising Faradaic efficiency of the reduction to metallic Fe^0 was achieved, amounting to ≈55%. The post-mortem XRD studies and microstructural characterisations have shown that the iron deposits obtained by the electroreduction of $Fe_{2.3}Mg_{0.7}O_4$ spinel suspension still contain trapped Mg^{2+}-containing species and initial spinel particles, although in a smaller amount as compared to the bulk approach. The electroreduction in suspension allowed to reach ≈20% Faradaic efficiency, being notably higher than that previously demonstrated in the literature even for stronger alkaline conditions. The obtained

findings are believed to open new pathways for recovering metallurgical waste with low content of magnesium impurities, as strongly encouraged by the European Commission.

ORCID

Daniela V. Lopes https://orcid.org/0000-0003-0652-5070
Aleksey D. Lisenkov https://orcid.org/0000-0001-7641-1883
Sergii A. Sergiienko https://orcid.org/0000-0002-3849-5681
Gabriel Constantinescu https://orcid.org/0000-0002-1614-1962
Artur Sarabando https://orcid.org/0000-0001-5919-8929
Margarida J. Quina https://orcid.org/0000-0002-9651-2427
Jorge R. Frade https://orcid.org/0000-0001-8445-2562
Andrei V. Kovalevsky https://orcid.org/0000-0001-5814-9797

References

1. M. Izaki, *Modern Electroplating*, ed. M. Schlesinger and M. Paunovic (Wiley, New Jersey, NJ) 5th ed., 11, p 309 (2010).
2. M. A. Quader, S. Ahmed, S. Z. Dawal, and Y. Nukman, *Renew. Sustain. Energy Rev.*, **55**, 537 (2016).
3. A. Allanore, H. Lavelaine, G. Valentin, J. P. Birat, and F. Lapicque, *J. Electrochem. Soc.*, **154**, E187 (2007).

4. B. Yuan, O. E. Kongstein, and G. M. Haarberg, *J. Electrochem. Soc.*, **156**, D64 (2009).
5. Q. Wang, Y. Zhu, Q. Wu, E. Gratz, and Y. Wang, *RSC Adv.*, **5**, 5501 (2015).
6. Y. A. Ivanova, J. F. Monteiro, A. L. Horovistiz, D. K. Ivanou, D. Mata, R. F. Silva, and J. R. Frade, *J. Appl. Electrochem.*, **45**, 515 (2015).
7. A. Allanore, H. Lavelaine, G. Valentin, J. P. Birat, and F. Lapicque, *J. Electrochem. Soc.*, **155**, E125 (2008).
8. A. Allanore, H. Lavelaine, G. Valentin, J. P. Birat, P. Delcroix, and F. Lapicque, *Electrochim. Acta*, **55**, 4007 (2010).
9. X. Zou, S. Gu, X. Lu, X. Xie, C. Lu, Z. Zhou, and W. Ding, *Metall. Mater. Trans. B*, **46B**, 1262 (2015).
10. Y. A. Ivanova, J. F. Monteiro, L. B. Teixeira, N. Vitorino, A. V. Kovalevsky, and J. R. Frade, *Mater. Des.*, **122**, 307 (2017).
11. K. K. Lee, S. Deng, H. M. Fan, S. Mhaisalkar, H. R. Tan, E. S. Tok, K. P. Loh, W. S. Chin, and C. H. Sow, *Nanoscale*, **4**, 2958 (2012).
12. A. Baklavaridis, K. Vatalis, K. Karayannis, P.-N. Benetis, and G. Charalampides, *Min. Miner. Depos.*, **15**, 11 (2021).
13. L. B. A. Negrão and M. L. da Costa, *J. South Am. Earth Sci.*, **108**, 103164 (2021).
14. P. D. Allen, N. A. Hampson, and G. J. Bignold, *J. Electroanal. Chem.*, **99**, 299 (1979).
15. P. D. Allen, N. A. Hampson, and G. J. Bignold, *J. Electroanal. Chem.*, **111**, 223 (1980).
16. P. D. Allen, G. J. Bignold, and N. A. Hampson, *J. Electroanal. Chem.*, **112**, 239 (1980).
17. Z. He, R. V. Gudavarthy, J. A. Koza, and J. A. Switzer, *J. Am. Chem. Soc.*, **133**, 12358 (2011).
18. J. F. Monteiro, Y. A. Ivanova, A. V. Kovalevsky, D. K. Ivanou, and J. R. Frade, *Electrochim. Acta*, **193**, 284 (2016).
19. V. Feynerol, H. Lavelaine, P. Marlier, M. N. Pons, and F. Lapicque, *J. Appl. Electrochem.*, **47**, 1339 (2017).
20. K. Čabanová, J. Vlček, J. Seidlerová, and V. Matějka, *Mater. Today Proc.*, **5**, S2 (2018).
21. L. Fu, H. Gu, A. Huang, M. Zhang, and J. Wu, *Ceram. Int.*, **46**, 959 (2020).
22. A. A. Yaremchenko, A. V. Kovalevsky, E. N. Naumovich, V. V. Kharton, and J. R. Frade, *Solid State Ionics*, **192**, 252 (2011).
23. A. V. Kovalevsky, A. A. Yaremchenko, E. N. Naumovich, N. M. Ferreira, S. M. Mikhalev, F. M. Costa, and J. R. Frade, *J. Eur. Ceram. Soc.*, **33**, 2751 (2013).
24. E. M. Domingues, E. V. Tsipis, A. A. Yaremchenko, F. M. Figueiredo, J. C. Waerenborgh, A. V. Kovalevsky, and J. R. Frade, *J. Eur. Ceram. Soc.*, **33**, 1307 (2013).
25. N. M. Ferreira, A. V. Kovalevsky, E. N. Naumovich, A. A. Yaremchenko, K. V. Zakharchuk, F. M. Costa, and J. R. Frade, *J. Eur. Ceram. Soc.*, **34**, 2339 (2014).
26. N. M. Ferreira, A. V. Kovalevsky, F. M. Costa, and J. R. Frade, *J. Am. Ceram. Soc.*, **99**, 1889 (2016).
27. F. Bræstrup and K. K. Hansen, *J. Solid State Electrochem.*, **13**, 1241 (2009).
28. J. Patil, D. Nadargi, I. S. Mulla, and S. S. Suryavanshi, *Mater. Lett.*, **213**, 27 (2018).
29. Y. Zu, Y. Zhao, K. Xu, Y. Tong, and F. Zhao, *Ceram. Int.*, **42**, 18844 (2016).
30. K. Randhir, N. R. Rhodes, L. Li, N. AuYeung, D. W. Hahn, R. Mei, and J. F. Klausner, *Sol. Energy*, **163**, 1 (2018).
31. N. M. Ferreira, A. V. Kovalevsky, M. C. Ferro, F. M. Costa, and J. R. Frade, *Ceram. Int.*, **42**, 11070 (2016).
32. D. V. Lopes, A. V. Kovalevsky, M. J. Quina, and J. R. Frade, *Ceram. Int.*, **44**, 20354 (2018).
33. S. W. Hughes, *Phys. Educ.*, **40**, 468 (2005).
34. D. V. Lopes, Y. A. Ivanova, A. V. Kovalevsky, A. R. Sarabando, J. R. Frade, and M. J. Quina, *Electrochim. Acta*, **327**, 135060 (2019).
35. V. Raghavan, *J. Phase Equilibria Diffus.*, **31**, 368 (2010).
36. N. Sato, K. Kudo, and T. Noda, *Corros. Sci.*, **10**, 785 (1970).
37. P. Schmuki, S. Virtanen, A. Davenport, and C. Vitus, *J. Electrochem. Soc.*, **143**, 574 (1996).
38. F. La Mantia, J. Vetter, and P. Novák, *Electrochim. Acta*, **53**, 4109 (2008).
39. J. T. S. Irvine, D. C. Sinclair, and A. R. West, *Adv. Mater.*, **2**, 132 (1990).
40. C. H. Hsu and F. Mansfeld, *Corrosion*, **57**, 747 (2001).
41. M. R. S. Abouzari, F. Berkemeier, G. Schmitz, and D. Wilmer, *Solid State Ionics*, **180**, 922 (2009).
42. M. Pourbaix, *Atlas of Electrochemical Equilibria in Aqueous Solutions* (National Association of Corrosion Engineers, Brussels) 2nd ed., p. 648 (1974).
43. A. Allanore, J. Feng, H. Lavelaine, and K. Ogle, *J. Electrochem. Soc.*, **157**, E24 (2010).
44. M. Siebentritt, P. Volovitch, K. Ogle, and G. Lefèvre, *Colloids Surfaces A Physicochem. Eng. Asp.*, **440**, 197 (2014).
45. J. A. M. LeDuc, R. E. Loftfield, and L. E. Vaaler, *J. Electrochem. Soc.*, **106**, 659 (1959).
46. J. M. Skowroński, T. Rozmanowski, and M. Osińska, *Process Saf. Environ. Prot.*, **93**, 139 (2015).
47. D. V. Lopes, A. Kovalevsky, M. Quina, and J. Frade, *J. Electrochem. Soc.*, **167**, 102508 (2020).